Energy-dense wire-like supercapacitors based on scalable three-dimensional porous metal-graphene oxide skeleton electrodes

Ruitao Zhou, Kwok Ho Lam*

Author Ruitao Zhou: Department of Electrical Engineering, Research Institute of Smart Energy, The Hong Kong Polytechnic University, Hong Kong, ruitzhou@polyu.edu.hk
Corresponding Author Kwok Ho Lam: Centre for Medical and Industrial Ultrasonics, James Watt School of Engineering, University of Glasgow, Glasgow, Scotland, United Kingdom, Kwokho.Lam@glasgow.ac.uk; Department of Electrical Engineering, Research Institute of Smart Energy, The Hong Kong Polytechnic University, Hong Kong

Abstract:
Synthesis of three-dimensional (3D) porous current collectors is a pioneering strategy to improve the energy density and power density of wire-like supercapacitors. The strategy is further promoted in this work by synthesizing multi-scale 3D porous current collectors with secondary nanostructured metals on the surface. Through the proposed nano 'reinforced concrete' mechanism at the micron scale, Ni and graphene oxide (GO) are synergistically co-deposited on the surface of Ni wires, forming a macroporous skeleton with tunable thickness. Cu is further synthesized on the Ni-GO macroporous skeleton through a structural catalyzed electroless deposition. The resultant Cu@Ni-GO exhibits a 3D porous structure covered with secondary Cu nanosheets. Cu@Ni-GO and Ni-GO are used as current collectors for negative and positive electrodes, respectively, while active materials are *in situ* formed on each electrode through surface oxidation. The negative electrodes and positive electrodes exhibit the excellent electrochemical performance with volumetric capacitances of 510.7 F/cm^3 and 235.2 F/cm^3, respectively. Asymmetric wire-like supercapacitors are also developed, showing a very high energy density of 30.2 mWh/cm^3. The application potential of wire-like supercapacitors is demonstrated by powering a LED array and an electronic watch.

Keywords: wire-like supercapacitor, Cu, Ni-GO, electroless deposition, structural catalysis, multi-scale

1 Introduction

Flexible energy storage devices have attracted increasing interest due to their significance in wearable electronics and functional clothes. Among various flexible energy storage devices, fiber/wire-like energy storage devices exhibit unique advantages due to their capability of being integrated and weaved into smart clothes. In this field, aqueous fiber/wire-like supercapacitors demonstrated relatively high

potential when compared to batteries in terms of safety, energy density and power density [1, 2]. However, the energy densities of state-of-the-art fiber/wire-like supercapacitors are not high, and sometimes even much lower than their counterparts of flat shape. Thus, the topic for improving the energy densities of fiber/wire-like supercapacitors is an urgent challenge in the research field of advanced nanotechnologies.

Flexible fiber/wire-like electrodes of supercapacitors usually consist of a flexible electrically conducting core and immobilized active materials, in which the core can be carbon-based fibers [3-5], metal coated fibers [6, 7] and metal wires [8-10]. Carbon fibers act as both conducting core and active materials, endowing the corresponding supercapacitors with simple structures and good electrochemical properties. Nevertheless, aqueous carbon-based fiber/wire-like supercapacitors have limited energy densities due to their low specific capacitance and narrow working potential window [11-13]. Metal oxide-based fiber/wire-like pseudosupercapacitors exhibited improved energy densities due to their high specific capacitance and relatively large working potential windows (1.5 – 2.0 V) [9, 14]. The fiber/wire-like electrodes were synthesized via *in situ* growth of nanostructured metal oxides on conducting current collectors through different methods such as electrochemical deposition [15, 16] and hydrothermal deposition [17, 18]. Nanostructured active materials often exhibit excellent specific capacitance due to their large specific surface areas and short electronic transfer path, but the mass loading of active materials is limited due to the thin nanostructured active materials.

To improve the energy density of fiber/wire-like supercapacitors, electrodes with 3D porous current collectors were synthesized. Compared to the simple conducting wires, 3D porous wire-like current collectors have much larger surface areas, and therefore can bear larger quantity of nanostructured active materials, leading to the elevated capacitance of total electrodes [19, 20]. A basic strategy of synthesizing 3D porous wire-like current collectors is to deposit 3D porous metal films on conducting wires, in which a 3D porous Ni film on Ni wires was synthesized through the bubble assisted electrodeposition, and then nanostructured metal oxides were further synthesized on the 3D porous substrates [21, 22]. As this kind of 3D porous Ni film was synthesized with the assistance of randomly generated hydrogen bubbles, the structural and mechanical properties cannot be well controlled. More advanced nanotechnologies are desired to synthesize 3D porous current collectors with controllable structures and properties.

In this work, 3D porous wire-like electrodes with tunable structure and thickness were synthesized through a nano ‘reinforced concrete’ strategy. Graphene oxide (GO) was adsorbed on the surface of activated Ni wires, and then the deposition of Ni quickly spread from Ni wires to the surface of GO. Thus, GO was immobilized on the surface of Ni wires in a 3D geometry. The synergistic deposition of GO and Ni was spontaneously repeated for many times, and the 3D macroporous Ni-GO was

eventually formed on the surface of Ni wires. The structure of wires was similar to that of reinforced concrete, in which Ni and GO functioned as the adhesive and the reinforced material, respectively. The thickness of the porous Ni-GO film was determined by the number of stacking layers of GO, and the porous Ni-GO layer can be built up to hundreds of microns. The macroporous Ni-GO layer functioned as the skeleton to synthesize Cu nanosheets through structural catalyzed electroless deposition. Both 3D porous Ni-GO skeleton and Cu nanosheets on the Ni-GO skeleton exhibited large surface areas, which were directly used as positive and negative electrodes, respectively. In an alkaline solution, $Ni(OH)_2$ and Cu_2O would be *in situ* formed as the active materials on the surface of Cu and Ni, respectively. The details of *in situ* formation of $Ni(OH)_2$ from Ni current collectors with large surface area can be referred to our previous work [23, 24]. Cu_2O was mostly reported as the positive electrode in literature [25, 26], but seldom as the negative electrode due to the large volume change (about 68%) during the redox process between Cu and Cu_2O. Nevertheless, electrodes with *in situ* formed active materials through surface oxidation could accommodate the volume change of active materials during the redox process [27]. Ascribed to the large surface area of multi-scaled 3D porous structure, the Cu@Ni-GO electrodes exhibited the excellent electrochemical performance with an areal capacitance of 4.47 F/cm^2. Asymmetry wire-like supercapacitors were fabricated, achieving a very high energy density of 30.2 mWh/cm^3.

2 Experiments

2.1 Materials

Nickel sulfate hexahydrate (Aladdin), palladium(II) chloride (Alfa Aesar), silver nitrate (International Laboratory of USA), copper sulfate pentahydrate (Aladdin), lactic acid (International Laboratory of USA), GO aqueous dispersion (Carmery), borane dimethylamine complex (DMAB) (Acros Organics), sodium hydroxide (International Laboratory of USA), potassium sodium tartrate tetrahydrate (Aladdin), palladium ammonium (International Laboratory of USA), sodium citrate dehydrate (Fisher), and formaldehyde solution (Macklin) were used as received.

2.2 Synthesis of Cu dendrites and Ni nanopheres

Cu and Ni were synthesized through the modified electroless deposition method reported in literature [28]. Ni wires with different diameters (0.2 mm, 0.1 mm and 0.05 mm) were immersed in 0.2% (w/w) $PdCl_2$ solution for 1 min to form a very thin Pd catalytic layer on the surface of Ni wires through the displacement reaction. The Ni wires bearing Pd catalyst were rinsed with de-ionized (DI) water, and then immersed in the Cu plating solution containing 52 mM $CuSO_4$, 300 mM NaOH, 100 mM potassium sodium tartrate and 115 mM HCHO. The reaction was carried out for 3 h, and then Cu dendrites were formed.

The Ni wires with Cu dendrites were rinsed with DI water, and then immersed in the Ni plating solution. The plating solution contained 14 mM nickel sulfate, 6.8 mM

sodium citrate, and 11 mM lactic acid, with the pH of 8.5 adjusted by adding ammonia solution. Ni was then plated on the surface of Cu dendrites. The plating reaction was slow in the initial stage for about 10 min, and hydrogen bubbles were adsorbed on the surface of Ni wires. In the second stage, the bubbles on the surface of Ni wire were suddenly exploded and the plating reaction thrived. The plating reaction in the second stage was carried out for several mins, and then Ni nanoclusters were formed on the surface of Cu dendrites.

2.3 Synthesis of Ni-GO macroporous structure

After synthesized Ni nanoclusters on Cu dendrites, the Ni wires had high catalytic activity for electroless deposition. The Ni wires bearing Ni nanoclusters on Cu dendrites were transferred to a Ni-GO co-deposition solution that was prepared by adding GO dispersion in the Ni plating solution. The GO concentration was 20 mg/mL, and the pH of the solution was adjusted to 7.5. The reaction was carried out for about 6 h, and then the Ni wires were rinsed with DI water. The macroporous Ni-GO was synthesized through the synergistic deposition of Ni and GO on the surface of Ni wires (NiW).

2.4 Synthesis of Cu nanosheets on macroporous Ni-GO

Ni wires with the macroporous Ni-GO were immersed in the same Cu plating solution for plating the first Cu layer. The reaction was carried out for 3 h. Then, Cu nanosheets were synthesized on the surface of macroporous Ni-GO.

2.5 Characterizations

The structures of Ni-GO@NiW and Cu@Ni-GO@NiW electrodes at different synthesis stages were characterized through scanning electron microscopy (SEM) (TESCAN VEGA3). The components on the surface of the electrodes were characterized by X-ray photoelectron spectroscopy (XPS) (Thermo ESCALAB 250XI), and the C1s peak was 286.2 eV.

2.6 Electrochemical tests

Ni-GO@NiW and Cu@Ni-GO@NiW were tested as positive and negative electrodes, respectively, while $Ni(OH)_2$ and Cu_2O active materials were *in situ* formed through the surface oxidation of the electrodes in alkaline electrolyte. The test was carried out on an electrochemical station (EC-Lab), and 1.5 M KOH was used as the electrolyte. Before tested as positive electrodes, Ni-GO@NiW was pretreated by immersing into 20 ppm $PdCl_2$ solution for 1 h to increase the surface roughness and area. Both electrodes were tested with a working length of 2.0 cm, and a Pt wire and Ag/AgCl were used as the counter electrode and reference electrode, respectively. Cyclic voltammetry (CV), galvanic charge discharge (GCD) and electro impedance spectroscopy (EIS) tests were carried out. Asymmetric supercapacitors were fabricated using Ni-GO@NiW and Cu@Ni-GO@NiW as positive and negative electrodes, respectively. Wire-like supercapacitors were fabricated by sealing two parallel electrodes in a silicone tube, and the ends were sealed by thermal shrinking

plastic tubes.

The specific capacitances of electrodes and devices were calculated through GCD curves by the following equations:

$$C_s = It/s\Delta V \quad (1)$$
$$C_v = It/v\Delta V \quad (2)$$

where C_s is the areal specific capacitance, C_v is the volumetric specific capacitance, I is the discharge current, t is the discharge time, s is the surface area of the electrodes, v is the volume of the total electrodes, and ΔV is the discharge potential window.

The energy density of supercapacitors was calculated through the integration of GCD discharge curves:

$$E_v = \int_0^t IU_{(t)}dt \quad (3)$$

where E_v is the volumetric energy density and $U_{(t)}$ is the discharge potential.

3 Results and Discussion

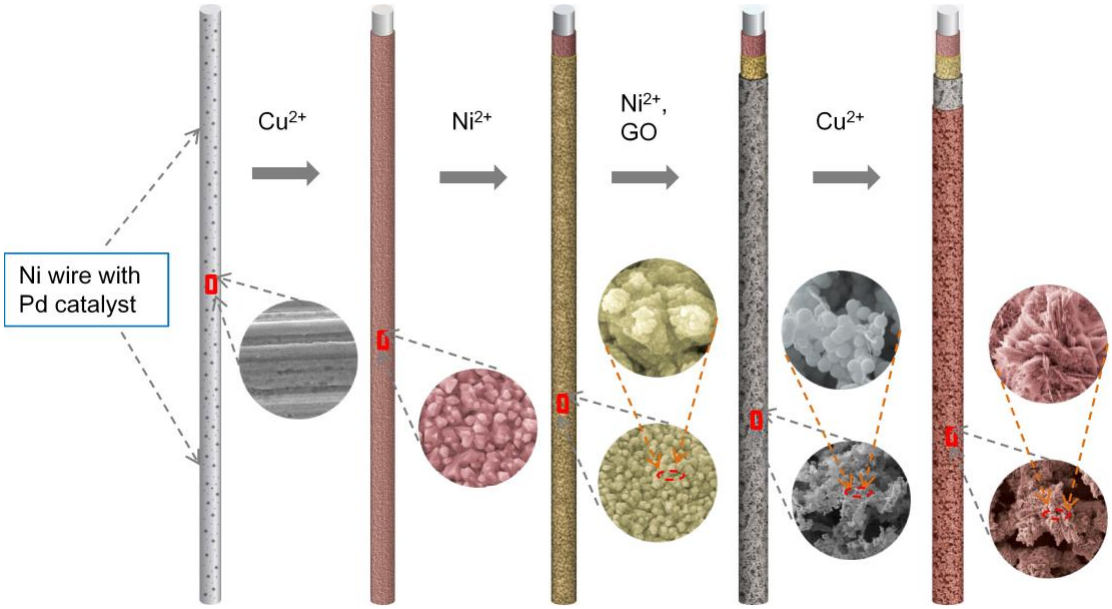

Figure 1 Scheme of the synthesis process of Cu@Ni-GO wire electrodes.

Macroporous electrodes with multi-scale nanostructures were synthesized through the sequential electroless deposition of Ni and Cu, which is shown in Figure 1. Cu dendrites, Ni nanoclusters, macroporous Ni-GO, and Cu nanosheets were sequentially formed on the surface of Ni wires via different mechanisms. The first layer of Cu dendrites and the second layer of Ni nanoclusters were formed through the ionic diffusion effect in the dilute plating solution, which were discussed in our previous

work [23]. The third layer of macroporous Ni-GO was formed through the nano 'reinforced concrete' mechanism in which Ni and GO were synergistically deposited on the surface. The 3D geometry of the GO assisted the formation of 3D porous Ni-GO. The fourth layer of Cu nanosheets was formed through the surface catalyzed electroless deposition mechanism, and the growth rate and direction were greatly affected by the Ni-GO substrate. The Cu dendrites and Ni nanoclusters were deposited on Ni wires to activate the surface of Ni wires, which were covered by the subsequent layers. The Cu nanosheets on porous Ni-GO skeleton had a 3D multi-scale structure enabling the Ni wires with large surface area. Ni wires bearing Cu nanosheets on macroporous Ni-GO skeleton (Cu@Ni-GO@NiW) would be the excellent current collectors due to the large surface area and efficient electronic transfer path.

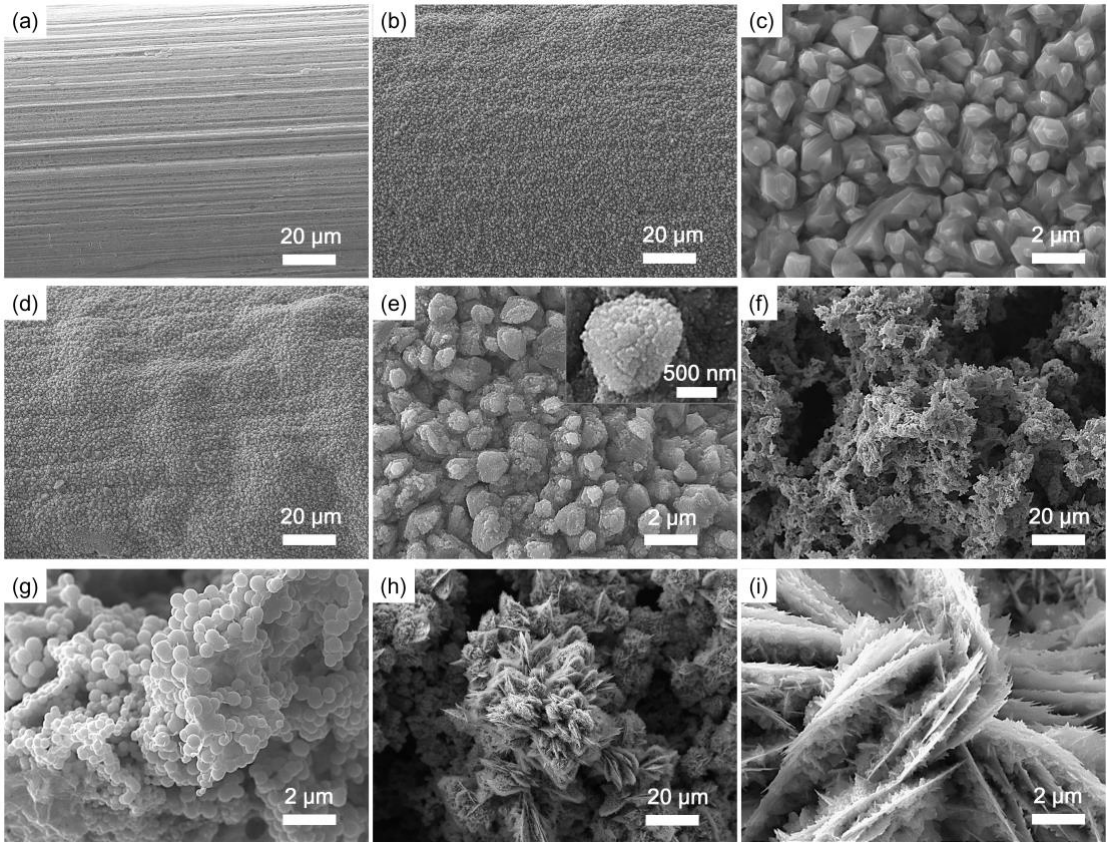

Figure 2 SEM images of (a) a pristine Ni wire and a Ni wire sequential deposited with (b, c) Cu dendrites, (d, e) Ni nanoclusters, (f, g) a Ni-GO macroporous skeleton with Ni nanopheres, and (h, i) Cu nanosheets with lateral dendrites.

Cu@Ni-GO@NiW had the 3D porous structure at micron scale and secondary Cu nanosheets at nano scale. The multi-scale structure of Cu@Ni-GO@NiW at different synthesis stages were characterized by SEM as shown in Figure 2. The pristine Ni wire exhibited a relative smooth surface (Figure 2a). With the diffusion-controlled Cu deposition in a low concentration of Cu^{2+} (~50 mM), the Cu dendrites with a height of several microns were formed and deposited on the Ni surface as shown in Figures 2b and c. If the diffusion of Cu^{2+} was interfered by strong agitation, irregular Cu clusters

were formed instead (Supporting information, Figure S1), suggesting the significance of Cu^{2+} diffusion in the formation of Cu dendrites. The second layer of Ni nanoclusters with the diameters of within 100 nm is shown in Figures 2d and e. The tinny Ni nanoclusters were formed throughout the surface of Cu dendrites, which was further confirmed by EDX mapping characterization (Supporting information, Figure S2). The Ni nanoclusters increased the surface roughness and area of Ni wires, facilitating the enhancement of the surface catalytic activity because metal surfaces with larger surface area and more sharp points would generally offer higher surface energy [29, 30].

Subsequently, macroporous Ni-GO was synthesized through the co-deposition of Ni and GO that was a synergistic process in which a balanced deposition rate of Ni and GO was required. The electroless deposition was carried out at a low concentration of Ni^{2+} (14 mM), and the deposition of Ni could not occur on the pristine Ni wires with the sole involvement of Pd catalyst. This indicates that the deposition of Ni could not occur only via the catalysis of pristine metal, so the catalytic effect should be improved by a special structural design. In this work, Ni wires with Ni nanoclusters on Cu dendrites were prepared as the substrate with high catalytic activity. In the synergistic deposition process, the deposition of Ni and GO was carried out via the 'reinforced concrete' mechanism in which Ni and GO functioned as the adhesive and reinforced material, respectively. The 3D geometry of GO endowed the resultant Ni-GO with the macroporous structure. Through the repeated alternative deposition of Ni and GO, the thickness of macroporous Ni-GO could be built up to hundreds of microns. The SEM images (Figures 2f and g) show that Ni nano hemispheres with diameters ranging from 200 nm to 500 nm were formed on the wall of the macroporous Ni-GO skeleton. The Ni nano hemispheres were formed through the diffusion effect of Ni ions in the synthesis process, which could greatly enlarge the surface area of macroporous Ni-GO layer. The surface area of the macroporous Ni-GO layer was evaluated through a double-layer method [23, 24]. Compared to the pristine Ni wire, the surface area of Ni wires with the macroporous Ni-GO layer (Ni-GO@NiW) was enlarged by 99.3 times (Supporting information, Figure S3). Though Ni-GO@NiW had the large surface area due to its 3D macroporous structure, its surface area can be further enhanced by depositing other nanostructured materials on the macroporous Ni-GO as a skeleton. With the deposition of Cu nanosheets on the macroporous Ni-GO skeleton, the resultant Cu@Ni-GO@NiW exhibited a 3D multi-scale structure as shown in Figures 2h and i. Besides the main Cu nanosheets with a thickness of ~5 μm, the secondary tinny Cu nanosheets with a thickness of 1 – 2 μm were grown laterally on the surface of main Cu nanosheets, resulting in the much larger surface area. Compared to the Ni wires with Cu dendrites on the first layer, the surface area of Cu@Ni-GO@NiW was improved by 14.4 times through the double-layer capacitance test (Supporting information, Figure S4) due to the 3D multi-scale porous structure.

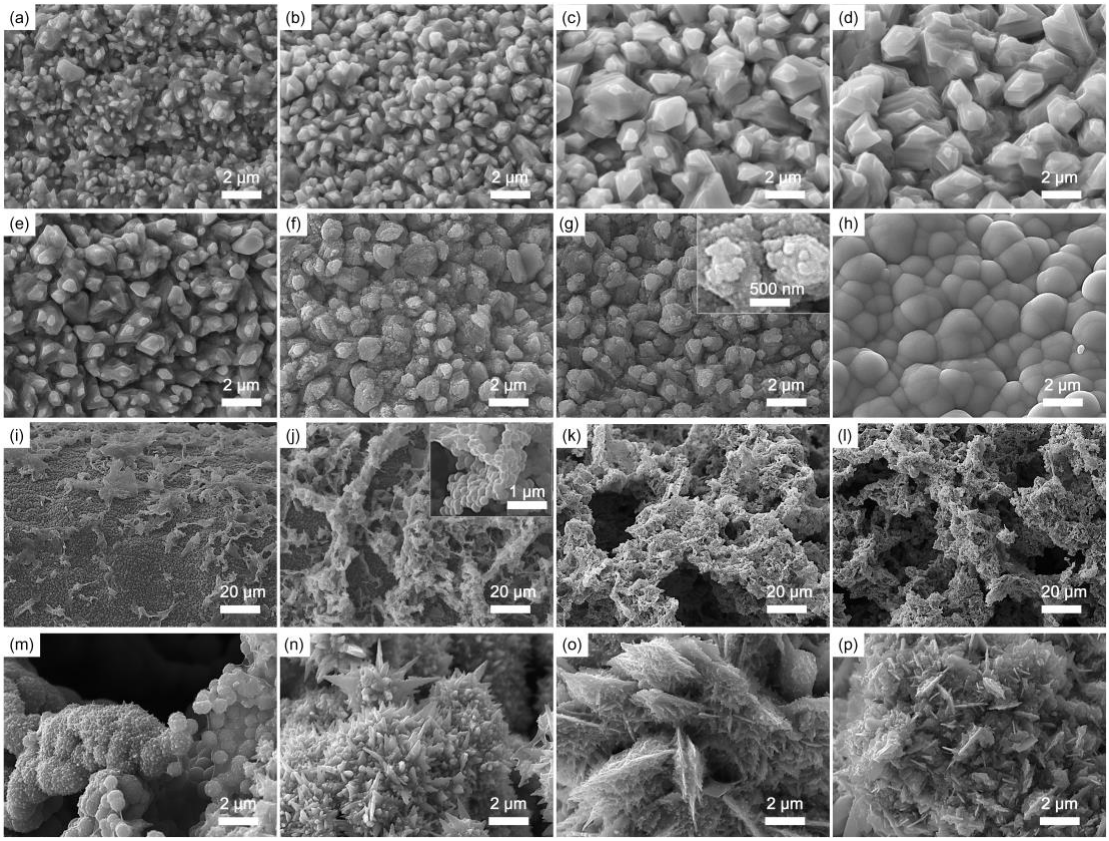

Figure 3 SEM images of the evolution of (a – d) Cu dendrites, (e – h) Ni nanoclusters, (i – l) macroporous Ni-GO structure, and (m – p) Cu sheets with lateral dendrites.

The Cu@Ni-GO@NiW with the 3D multi-scale porous structure was synthesized through a series of spontaneous growth process, and the detailed structural evolution in each stage is displayed by a series of SEM images (Figure 3). For the first layer of Cu dendrites, the electroless deposition of Cu was initiated by the Pd catalyst on the Ni wires, and then sustained through the self-catalysis mechanism by the initially deposited Cu. The deposition of Cu on the surface of Ni wires was a non-uniform process under the condition of low concentration of Cu^{2+} without agitation due to diffusion effect. When the deposition reaction was carried out for 1 h, tiny Cu protrusions with the size of ~200 nm and prismatic shape appeared (Figure 3a). The tip of Cu protrusions grew faster than the surrounding areas, and the Cu protrusions enlarged as the reaction time was prolonged. When the reaction was carried out for 3 h, the Cu dendrites with the height of several microns were formed (Figure 3c). The Cu dendrites had no apparent change in size and shape even the deposition process

was further extended up to 6 h, indicating that the deposition of Cu reached equilibrium. It should be noted that through observing the generation of CO_2 bubbles as a byproduct during the Cu deposition process, the deposition process was greatly accelerated when the Cu dendrites were formed, indicating that the Cu dendrites exhibited an additional catalytic effect for the electroless deposition.

Though the Ni wires with Cu dendrites exhibited the improved catalytic activity due to the larger surface areas and more sharp points, the electroless deposition of Ni on Ni wires with Cu dendrites still could not happen at the designed pH condition (pH = 7.5). To further improve the surface catalytic activity for the electroless deposition of Ni, Ni nanoclusters was synthesized on the surface of Cu dendrites at the slightly higher pH condition (pH = 8.5) (Figures 3e – h). The formation of Ni nanoclusters was a two-stage process. In the first stage, the reaction rate was very slow, and no apparent change on the surface could be observed. Besides, all the generated hydrogen gas was adsorbed on the surface of Ni wires such that no bubble was observed in the solution. The quiet reaction lasted for ~10 min. In the second stage, the accumulated hydrogen gas suddenly exploded throughout the surface of Ni wires. The generation of hydrogen bubbles was extremely vigorous, and the color of the surface quickly changed from brown to pale, indicating the significant increased deposition rate of Ni. With the fast deposition of Ni, the Ni nanoclusters were formed within several tens of seconds (Figures 3f – g). The Ni nanoclusters enlarged as the reaction time was prolonged, which were finally immerged with each other and formed Ni microclusters. When compared with Ni nanoclusters on Cu dendrites, the Ni microclusters had weaker catalytic activity due to their reduced sharp points and surface area.

With the integration of pristine catalysis by metal atoms and structural catalysis by Ni nanoclusters on the Cu dendrites, the co-deposition of Ni and GO was successfully carried out. At the initial stage, GO was physically adsorbed on the surface, and then Ni quickly spread on the GO surface from the Ni wires as shown in Figures 3i – l. Consequently, the physically adsorbed GO was firmly immobilized by the Ni film, and the 3D geometry of GO endowed the Ni-GO assembly with a 3D porous structure. As the processes of physical adsorption of GO and immobilization by Ni repeated, the Ni-GO assembly stacked on the surface and formed the macroporous Ni-GO skeleton. The thickness of porous Ni-GO was determined by the reaction (deposition) time, which could reach hundreds of microns.

The macroporous Ni-GO with large surface area was used as a substrate to grow the nanostructured Cu. The Ni-GO layer not only had the large surface area, but also the high catalytic activity. On the contrary to the Cu dendrites formed on the pristine Ni wires, Cu nanosheets were formed on the surface of porous Ni-GO under the same synthesis condition (Figures 3m – p, and Supporting information, Figure S5). The results demonstrated that the structural catalysis effect of the macroporous Ni-GO skeleton greatly affected the final structure of the nanostructured Cu. Ascribed to the

high catalytic activity of the Ni-GO substrates, Cu grew rapidly and exhibited a sharp needle structure at the first 40 mins (Figure 3n). Then, Cu grew two-dimensionally (2D) and formed the nanosheet structure at the reaction time of 1 h (Figure 3o). As the reaction time further prolonged, the nanosheet structure retained.

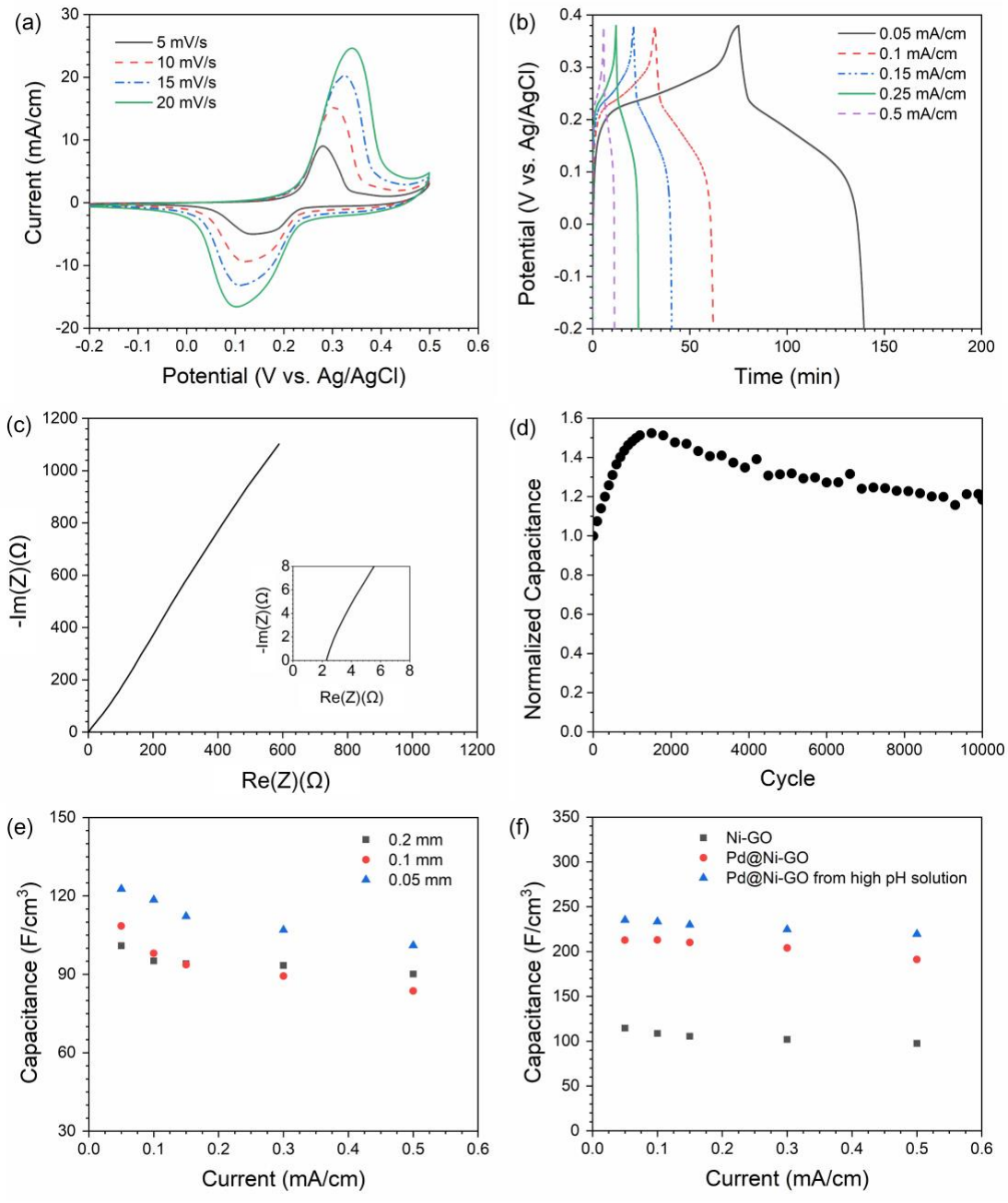

Figure 4 Electrochemical performance of Ni-GO positive electrodes: (a) CV curves at different scan rates, (b) GCD curves at different current densities, (c) EIS curve (inset: EIS curve at the high-frequency region), (d) long cycle performance with CV test at the scan rate of 10 mV/s, (e) volumetric capacitance of electrodes synthesized by Ni wires with different diameters, and (f) volumetric capacitance of Ni-GO and Pd@Ni-GO electrodes synthesized at different pH conditions.

With the large surface area, the macroporous Ni-GO@NiW was expected to be a good current collector. When Ni-GO@NiW was immersed in an alkaline electrolyte, $Ni(OH)_2$ active material was *in situ* formed due to the surface oxidation of Ni. The resultant $Ni(OH)_2$@Ni-GO@NiW was tested as positive electrodes, and the electrochemical performance is shown in Figure 4. Redox peaks in CV curves (Figure 4a) indicate that the capacitance of $Ni(OH)_2$@Ni-GO@NiW electrodes was mainly originated from the faradic mechanism. Through GCD test with different current densities (Figure 4b), the $Ni(OH)_2$@Ni-GO@NiW electrode exhibited good linear specific capacitances of 0.285, 0.269, 0.266, 0.264, 0.255 F/cm at the current densities of 0.05, 0.10, 0.15, 0.25, 0.50 mA/cm, respectively. The 0.6 mm-diameter $Ni(OH)_2$@Ni-GO@NiW electrodes had areal specific capacitances of 1.51, 1.43, 1.41, 1.40 and 1.35 F/cm^2 at the current densities of 0.26, 0.53, 0.80, 1.33 and 2.65 mA/cm^2, respectively. 89% of capacitance could be retained even when the current density was increased by 10 times, indicating that the electrode had a very good rate capability. The serial equivalent resistance (ESR) of Ni-GO electrode was 1.8 Ω according to the x-axial intercept of the EIS curve (Figure 4c). No apparent semi-circle was observed at the high-frequency region, indicating that the charge transfer resistance was very small. The high rate capability and low resistance of the electrode were ascribed to (1) the *in situ* formed active materials led to intimate contact between active materials and current collectors, and (2) the 3D porous structure of current collector facilitated the fast ionic transfer between electrolyte and active materials. Due to the high accommodation to the volume change of active materials during the charge and discharge processes, the *in situ* formed $Ni(OH)_2$ active materials also facilitated the long cycle performance of the electrodes. The long cycle performance of $Ni(OH)_2$@Ni-GO@NiW electrodes was characterized by a continuous CV test up to 10,000 cycles. As shown in Figure 4d, 118 % of original capacitance was retained.

The highest volumetric capacitance of $Ni(OH)_2$@Ni-GO@NiW electrode was 100.9 F/cm^3, but can still be improved because the crystalline $Ni(OH)_2$ has the much higher theoretical capacitance (6563.6 F/cm^3). An efficient method for further improving the capacitance is to increase the volumetric ratio of $Ni(OH)_2$ and decrease the volumetric ratio of other materials and spacing. The Ni wire core and macropores occupied most of the dead volume that did not directly contribute to the capacitance of electrodes. The first approach was to reduce the volume ratio of the Ni wire core by employing the Ni wires with smaller diameters. Ni wires with small diameters (100 and 50 μm) were used as the substrate to synthesize the $Ni(OH)_2$@Ni-GO@NiW electrodes for the comparison of volumetric capacitance (Figure 4e and Supporting information Figure S6). As the diameters of Ni wires decreased from 200 μm to 100 μm and 50 μm, the volumetric capacitance of electrodes increased from 100.9 F/cm^3 to 108.5 and 122.7 F/cm^3, respectively. This was consistent with the decreasing trend of volume ratio of Ni wires (11.1%, 4.9% and 3.0%, respectively). According to the EIS curves of electrodes (Supporting information, Figure S7), all the electrodes had very low ESR, suggesting that the $Ni(OH)_2$@Ni-GO@NiW electrodes had high electrical

conductivity in both axial and lateral directions even though the diameter of the conducting core was reduced. The second approach was to reduce the volume ratio of pores and increase the volume ratio of Ni-GO in the porous Ni-GO layer simultaneously. The work was carried out by adjusting the pH value of the plating solution that could affect the deposition rate of Ni. The synergistic co-deposition of Ni and GO could only occur within a narrow pH region between 7.0 and 9.0. In the observation of experiments, the pH values of 7.5 – 8.0 were most suitable for the formation of robust macroporous Ni-GO structure, so the pH values of 7.5 and 8.0 were chosen to synthesize the electrodes for comparison. Though the electrodes synthesized at different pH values showed the similar macroporous structure (Supporting information, Figure S8), the density of GO layer increased from 0.426 g/cm^3 to 0.495 g/cm^3 when the pH value increased from 7.5 to 8.0. Correspondingly, the volumetric capacitance of the electrode increased by 35.9 % and reached 155.7 F/cm^3 by GCD test (Supporting information, Figure S9).

As the active material of $Ni(OH)_2$@Ni-GO@NiW electrodes was *in situ* generated from the surface oxidation, the surface area and morphology directly affected the capacitance of electrodes. To further improve the surface area of electrodes, one of facile approaches is to etch the surface by noble metal ions. Thus, the porous Ni-GO skeleton was slighted etched by dilute Pd ions through the galvanic displacing reaction. After etching, a thin Pd layer was formed on the surface of Ni-GO skeleton, which was evidenced by EDX and XPS characterizations (Supporting formation, Figures S10 and S11). The surface morphologies of the Ni-GO skeleton before and after etching are compared in Figure S12 (Supporting information), which show that Ni nano hemispheres were partly etched away and Pd nanoclusters with the size of 50 – 100 nm were formed on the surface. The effect of Pd etching was further studied through etching a Ni wire with the same condition. After removed the Pd layer from the surface of Ni wire with the sonication treatment in DI water, the surface area of the etched Ni wire was enlarged by 228.7 % (Supporting information, Figure S13). The GCD test results (Figure 4f and Supporting information, Figure S14a) show that the capacitance of the etched $Ni(OH)_2$@Ni-GO@NiW electrodes was improved by 51.0 %, reaching 235.2 F/cm^3. Besides, 103.8% of capacitance of etched $Ni(OH)_2$@Ni-GO@NiW electrodes was retained after 6,600 cycles of continuous CV test (Supporting information, Figure S14b), indicating that the long cycle performance of electrodes was not deteriorated by the Pd etching.

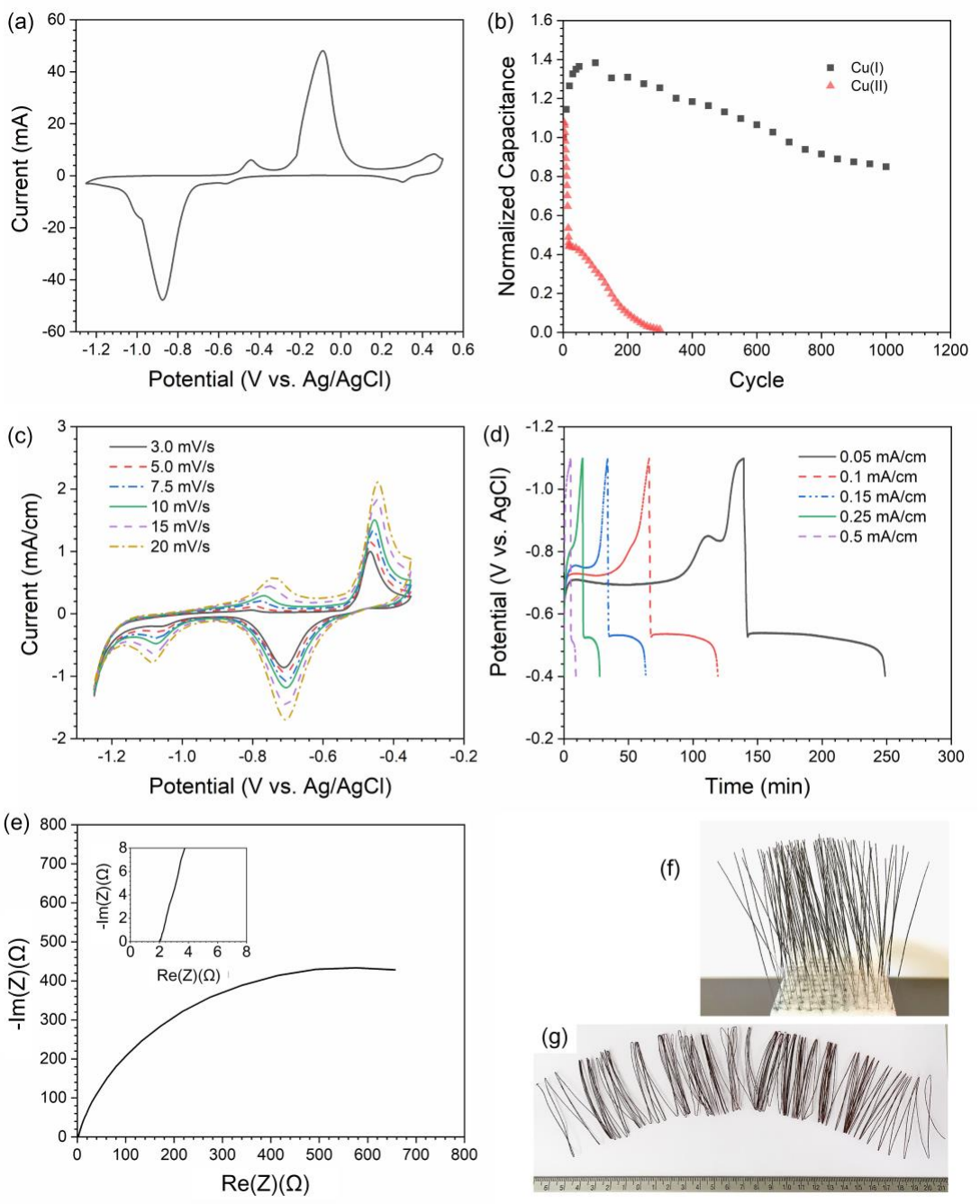

Figure 5 Electrochemical performance of Cu@Ni-GO@NiW electrodes: (a) CV curves with the full potential range at the scan rate of 5 mV/s, (b) long cycle performance with the potential range relative to the formation of Cu(I) (-1.25 – -0.35 V) and Cu(II) (-1.25 – 0.10 V), (c) CV curves at different scan rates, (d) GCD curves at different current densities, (e) EIS curve (inset: EIS curve at the high-frequency region), (f) photo of 100 separated Ni-GO@NiW electrodes, and (g) photo of a 10 m-long Cu@Ni-GO@NiW electrode.

The multi-scale 3D porous Cu@Ni-GO@NiW was also used as the current collectors, in which the surface of Cu can be oxidized into Cu_2O and CuO in the alkaline solution at low negative potential [31]. The electrochemical performance of

Cu@Ni-GO@NiW is shown in Figure 5. Figure 5a shows the CV curve of Cu@Ni-GO@NiW electrodes with the potential ranging from the negative to positive region. Two oxidation peaks at -0.45 V and -0.1 V were observed in the CV curve, corresponding to the formation of Cu(I) and Cu(II) ions, respectively [32]. The reversibility in the formation of Cu(I) and Cu(II) ions was investigated by adjusting the redox potential. The scan potential range between -1.25 – -0.35 V corresponds to the Cu/Cu(II) redox reaction, while the scan potential range between -1.25 – 0.10 V corresponds to the Cu/Cu(I) reaction. According to the long cycle test as shown in Figure 5b, the Cu/Cu(II) redox reaction showed the very poor reversibility, in which 56% of capacity was lost in the first 20 cycles and 90% of capacitance was degraded after 200 cycles. On the contrary, the Cu/Cu(I) redox reaction exhibited the very good reversibility that 85% of capacitance was retained at the end of 1,000 cycles. The difference is mainly attributed to the less volume change (68.1%) in the Cu/Cu(I) redox reaction when compared to the Cu/Cu(II) redox reaction (77.8%). Besides, another reason is that much less Cu atoms participated in the Cu/Cu(I) redox reaction at the low potential, which is indicated by the much smaller peak area of Cu/Cu(I) than that of Cu/Cu(II) in the CV curve as shown in Figure 5a.

The good reversibility of the Cu/Cu(I) redox reaction endowed the Cu@Ni-GO@NiW electrodes with the excellent electrochemical performance as negative electrodes. The CV curves of Cu@Ni-GO@NiW electrodes at different scan rates are shown in Figure 5c. Besides the main oxidation peak at -0.45 V, there was a negative oxidation peak at -0.75 V corresponding to the physically adsorbed oxygen [32, 33]. The GCD curves of electrodes at different current densities (Figure 5d) show that the linear capacitances were 0.45, 0.47, 0.41, and 0.31 F/cm at the current densities of 0.05, 0.1, 0.15, and 0.25 F/cm, respectively. The areal capacitances of the 0.35 mm-diameter electrode were 4.47, 4.26, 3.77, and 2.85 F/cm^2 at the current densities of 0.45, 0.9, 1.36 and 2.27 mA/cm^2, respectively. The high specific capacitance of the Cu@Ni-GO@NiW electrode was ascribed to the multi-scale porous structures. Moreover, the Cu@Ni-GO@NiW electrode had a small ESR of 2.0 Ω as shown in Figure 5e, indicating the good electrical conductivity of the electrode.

The synthesis process of both Cu@Ni-GO@NiW negative electrodes and $Ni(OH)_2$@Ni-GO@NiW positive electrodes were highly scalable, which was demonstrated by the prototypes of 100 individual electrodes (Figure 5f) and a 10 m-long electrode (Figure 5g). There was no extra difficulty to develop the 3D porous electrodes in large number or long length using the sequential multi-step structural catalyzed electroless deposition.

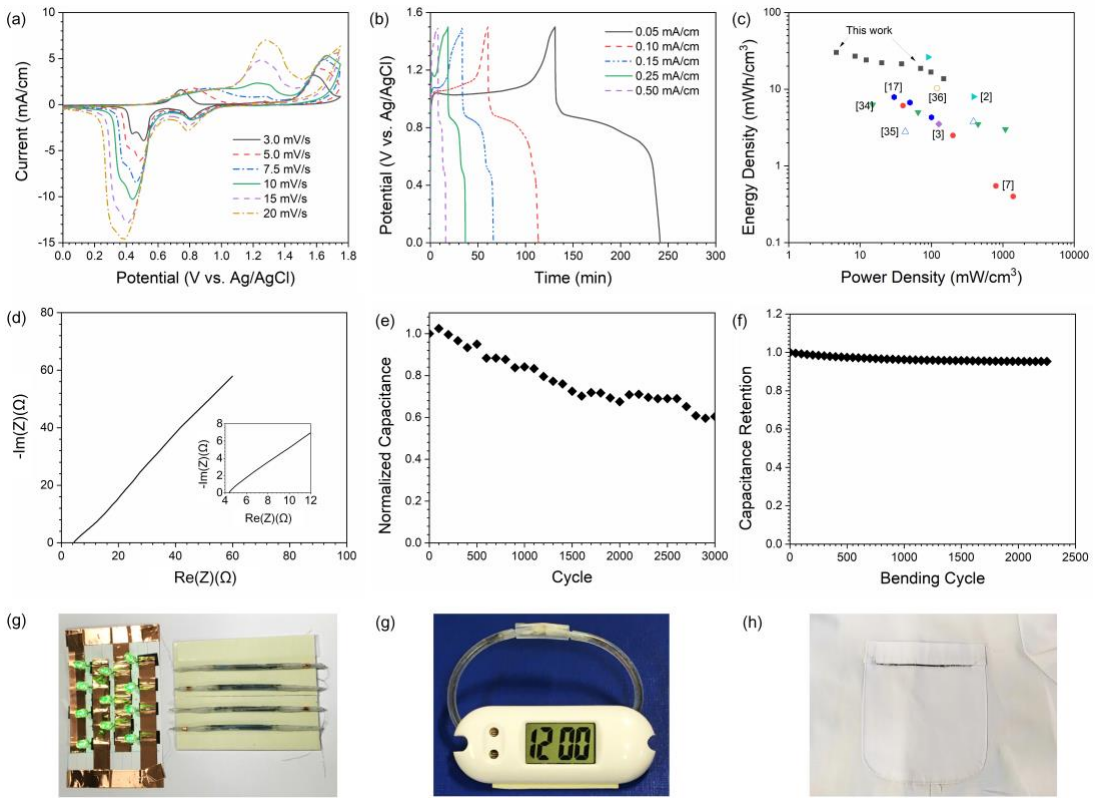

Figure 6 Electrochemical performance of Ni-GO//Cu@Ni-GO supercapacitor: (a) CV curves at different scan rates, (b) GCD curves at different current densities, (c) Ragone plot of this work and other reported work on wire-like supercapacitors, (d) EIS plots (inset: EIS curve at the high-frequency region), (e) long cycle performance at the scan rate of 10 mV/s, (f) bending test result of wire-like supercapacitors against the bending cycle, (g) demonstration of lighting a LED array by four serial-connected supercapacitors, (h) demonstration of powering up an electronic watch by two serial-connected supercapacitors, and (i) photo of a supercapacitor integrated on clothes as a trim.

$Ni(OH)_2$@Ni-GO@NiW//Cu@Ni-GO@NiW asymmetric supercapacitors were fabricated using $Ni(OH)_2$@Ni-GO@NiW and Cu@Ni-GO@NiW as positive and negative electrodes, respectively, with 1.5 M KOH solution as the electrolyte. The electrochemical performance of the supercapacitor is shown in Figure 6. The CV curves at different scan rates in Figure 6a show the apparent redox peaks mainly ascribed to the faradic mechanism. Figure 6b shows that the supercapacitor exhibited linear capacitances of 0.22, 0.21, and 0.20 F/cm at the current densities of 0.05 mA/cm, 0.10 mA/cm, and 0.15 mA/cm, respectively. Through doing the integration of discharge curves, the supercapacitor had very high energy densities of 30.2, 27.0, and 24.1 mWh/cm^3 at the power densities of 4.66, 8.51, and 12.2 mW/cm^3, respectively. As shown in the Ragone plot (Figure 6c), the $Ni(OH)_2$@Ni-GO@NiW//Cu@Ni-GO@NiW supercapacitor exhibited the much higher energy density than the recently reported wire-like supercapacitors such as CNT yarn supercapacitors (3.52 mWh/cm^3) [3], CNT/GO microfiber supercapacitors

(6.3 mWh/cm^3) [34], ppy@steel yarns supercapacitors (3.8 mWh/cm^3) [35], rGO@Ni threads supercapacitors (6.1 mWh/cm^3) [7], alginate/PEDOT:PSS@ppy supercapacitors (10.3 mWh/cm^3) [36], graphene/MnO_2 hybride supercapacitors (7.9 mWh/cm^3) [17], and $Ti_3C_2T_x$ supercapacitors (26.2 mWh/cm^3) [2]. According to the x-axial intercept of EIS curve (Figure 6c), the supercapacitor had an ESR of 4.4 Ω, which was consistent with the sum of the ESRs of both electrodes. The low ESR indicates that the device exhibited efficient electronic transportation paths throughout the 3D porous structures. The long cycle performance of the $Ni(OH)_2$@Ni-GO@NiW//Cu@Ni-GO@NiW supercapacitor was characterized by running the CV test continuously for 3,000 cycles (Figure 6e). It was found that 84% and 60% of capacitance were retained after 1,000 and 3,000 charge-discharge cycles, respectively.

The flexibility of the supercapacitor was tested by bending the device with different angles (Supporting information, Figure S15) and cycles (Figure 6f). The performance of supercapacitor showed no apparent degradation even bent up to 180 degree. 95% of the capacitance could be retained after continuously bent for more than 2,000 times. Furthermore, when the supercapacitor was bent with a large radius of curvature (1.5 cm), the capacitance showed no degradation after 5,000 times as shown in Figure S16 (Supporting information). Interestingly, the capacitance was found to slightly increase after cyclic bending. The reason is that the structural damage of the electrodes is minimized when the bending test is carried out at large radii of curvature, while the ionic transfer between the electrolyte and the electrode could be accelerated during the bending process. The application potential of the supercapacitor was demonstrated by powering a 11-LEDs array and an electronic watch (Figures 6g and h, respectively). The supercapacitor with the thinnest Ni current collector was mounted on clothes as a trim, suggesting that the wire-like supercapacitors are suitable to be integrated on smart clothes as energy storage devices.

4 Conclusion

With using the multi-step structural catalyzed electroless deposition method, the multi-scale 3D porous Cu@Ni-GO@NiW electrodes were synthesized successfully. After performed the four-step electroless deposition, Cu dendrites, Ni nanoclusters, macroporous Ni-GO skeleton, and Cu nanosheets were sequentially synthesized on the surface of Ni wires. The Cu dendrites and Ni nanoclusters were formed via the diffusion-controlled deposition mechanism, which were used to enhance the structural catalytic effect of the Ni surface. The macroporous Ni-GO skeleton was synthesized through the synergistic co-deposition of Ni and GO via the idea of nano ‘reinforced concrete’. Ni and GO were alternatively deposited on the surface, which served the functions of adhesion and reinforcement, respectively. The Cu nanosheets were further synthesized on the surface of porous Ni-GO skeleton via the structural catalyzed electroless deposition. It should be noted that the Ni-GO skeleton accelerated and directed the growth of Cu. The 3D porous Ni-GO skeleton and Cu@Ni-GO were directly used as positive and negative electrodes, respectively, while

$Ni(OH)_2$ and Cu_2O active materials were *in situ* formed by the surface oxidation of current collectors in KOH electrolyte. The resultant Ni-GO@NiW positive electrode and Cu-Cu_2O@Ni-GO@NiW negative electrode exhibited the excellent electrochemical performance with the volumetric capacitances of 235.2 F/cm^3 and 510.7 F/cm^3, respectively. The aqueous asymmetric supercapacitors were synthesized using the developed electrodes, reaching the very high volumetric energy density of 30.2 mWh/cm^3. Moreover, the wire-like supercapacitors were fabricated and sealed in plastic tubes to demonstrate the potential on applications by igniting a 11-LEDs array and powering an electronic watch.

Supporting information

Supporting information is available.

Acknowledgements

This work was supported financially by the Hong Kong Polytechnic University and the University of Glasgow.

References

[1] J. Ren, Y. Zhang, W. Bai, X. Chen, Z. Zhang, X. Fang, W. Weng, Y. Wang, H. Peng, Elastic and Wearable Wire-Shaped Lithium-Ion Battery with High Electrochemical Performance *Angew. Chem. Int. Edit.* **2014** 53, 7864-7869.

[2] Q. Liu, A. Zhao, X. He, Q. Li, J. Sun, Z. Lei, Z.-H. Liu, Full-Temperature All-Solid-State Ti_3C_2Tx/Aramid Fiber Supercapacitor with Optimal Balance of Capacitive Performance and Flexibility *Adv. Funct. Mater.* **2021** 31, 2010944.

[3] C. Choi, J.A. Lee, A.Y. Choi, Y.T. Kim, X. Lepró, M.D. Lima, R.H. Baughman, S.J. Kim, Flexible Supercapacitor Made of Carbon Nanotube Yarn with Internal Pores *Adv. Mater.* **2014** 26, 2059-2065.

[4] C. Wang, K. Hu, W. Li, H. Wang, H. Li, Y. Zou, C. Zhao, Z. Li, M. Yu, P. Tan, Z. Li, Wearable Wire-Shaped Symmetric Supercapacitors Based on Activated Carbon-Coated Graphite Fibers *ACS Appl. Mater. Inter.* **2018** 10, 34302-34310.

[5] X. Dong, J. Liang, H. Li, Z. Wu, L. Zhang, Y. Deng, H. Yu, Y. Tao, Q.-H. Yang, Matching electrode lengths enables the practical use of asymmetric fiber supercapacitors with a high energy density, *Nano Energy* **2021** 80, 105523.

[6] J. Bae, M.K. Song, Y.J. Park, J.M. Kim, M. Liu, Z.L. Wang, Fiber Supercapacitors Made of Nanowire-Fiber Hybrid Structures for Wearable/Flexible Energy Storage *Angew. Chem. Int. Edit.* **2011** 50, 1683-1687.

[7] L. Liu, Y. Yu, C. Yan, K. Li, Z. Zheng, Wearable energy-dense and power-dense supercapacitor yarns enabled by scalable graphene–metallic textile composite electrodes *Nat. Commun.* **2015** 6, 7260.

[8] T. Purkait, G. Singh, D. Kumar, M. Singh, R.S. Dey, High-performance flexible supercapacitors based on electrochemically tailored three-dimensional reduced graphene oxide networks *Sci. Rep-UK* **2018**

8, 640.
[9] Y. Huang, H. Hu, Y. Huang, M. Zhu, W. Meng, C. Liu, Z. Pei, C. Hao, Z. Wang, C. Zhi, From Industrially Weavable and Knittable Highly Conductive Yarns to Large Wearable Energy Storage Textiles *ACS Nano* **2015** 9, 4766-4775.
[10] Y. Guo, X. Hong, Y. Wang, Q. Li, J. Meng, R. Dai, X. Liu, L. He, L. Mai, Multicomponent Hierarchical Cu-Doped NiCo-LDH/CuO Double Arrays for Ultralong-Life Hybrid Fiber Supercapacitor *Adv. Funct. Mater.* **2019** 29, 1809004.
[11] X. Zhao, B. Zheng, T. Huang, C. Gao, Graphene-based single fiber supercapacitor with a coaxial structure *Nanoscale* **2015** 7, 9399-9404.
[12] Q. Meng, H. Wu, Y. Meng, K. Xie, Z. Wei, Z. Guo, High-performance all-carbon yarn micro-supercapacitor for an integrated energy system, *Adv. Mater. (Deerfield Beach, Fla.)* **2014** 26, 4100-6.
[13] Z. Lu, R. Raad, F. Safaei, J. Xi, Z. Liu, J. Foroughi, Carbon Nanotube Based Fiber Supercapacitor as Wearable Energy Storage *Front. Mater.* **2019** 6.
[14] C. Choi, H.J. Sim, G.M. Spinks, X. Lepró, R.H. Baughman, S.J. Kim, Elastomeric and Dynamic MnO_2/CNT Core–Shell Structure Coiled Yarn Supercapacitor *Adv. Energy. Mater.* **2016** 6, 1502119.
[15] X. Cheng, J. Zhang, J. Ren, N. Liu, P. Chen, Y. Zhang, J. Deng, Y. Wang, H. Peng, Design of a Hierarchical Ternary Hybrid for a Fiber-Shaped Asymmetric Supercapacitor with High Volumetric Energy Density *J. Phys. Chem. C* **2016** 120, 9685-9691.
[16] L. Gao, J.U. Surjadi, K. Cao, H. Zhang, P. Li, S. Xu, C. Jiang, J. Song, D. Sun, Y. Lu, Flexible Fiber-Shaped Supercapacitor Based on Nickel–Cobalt Double Hydroxide and Pen Ink Electrodes on Metallized Carbon Fiber *ACS Appl. Mater. Inter.* **2017** 9, 5409-5418.
[17] S.-W. Zhang, B.-S. Yin, C. Liu, Z.-B. Wang, D.-M. Gu, A low-cost wearable yarn supercapacitor constructed by a highly bended polyester fiber electrode and flexible film *J. Mater. Chem. A* **2017** 5, 15144-15153.
[18] F. Qi, H. Li, F. Yang, Z. Sun, Core−shell coaxially structured NiCo2S4@TiO2 nanorod arrays as advanced electrode for solid-state asymmetric supercapacitors *Nanotechnology* **2021** 32, 295705.
[19] S.-I. Kim, S.-W. Kim, K. Jung, J.-B. Kim, J.-H. Jang, Ideal nanoporous gold based supercapacitors with theoretical capacitance and high energy/power density *Nano Energy* **2016** 24, 17-24.
[20] X. Lang, A. Hirata, T. Fujita, M. Chen, Nanoporous metal/oxide hybrid electrodes for electrochemical supercapacitors *Nat. Nanotechnol.* **2011** 6, 232-236.
[21] K.-N. Kang, A. Ramadoss, J.-W. Min, J.-C. Yoon, D. Lee, S.J. Kang, J.-H. Jang, Wire-Shaped 3D-Hybrid Supercapacitors as Substitutes for Batteries *Nano-Micro Lett.* **2020** 12, 28.
[22] A. Sharifi, M. Arvand, S. Daneshvar, A novel flexible wire-shaped supercapacitor with enhanced electrochemical performance based on hierarchical $Co(OH)_2$@$Ni(OH)_2$ decorated porous dendritic Ni film/Ni wire *J. Alloy. Compd.* **2021** 856, 158101.
[23] R. Zhou, Y. Fu, K.-a. Chao, C.-H. Cheng, Green synthesis of nanoarchitectured nickel fabrics as high performance electrodes for supercapacitors *Renew. Energ.* **2019** 135, 1445-1451.
[24] R. Zhou, Y. Li, K.H. Lam, Scalable electrode materials with nanoporous current collector shells for supercapacitors with ultrahigh areal and volumetric capacitances, *J. Mater. Chem. A* **2021** 9, 21302-21312.
[25] C. Dong, Y. Wang, J. Xu, G. Cheng, W. Yang, T. Kou, Z. Zhang, Y. Ding, 3D binder-free Cu_2O@Cu nanoneedle arrays for high-performance asymmetric supercapacitors *J. Mater. Chem. A* **2014** 2, 18229-18235.

[26] P. Marathey, S. Khanna, R. Pati, I. Mukhopadhyay, A. Ray, Low temperature–controlled synthesis of hierarchical $Cu_2O/Cu(OH)_2/CuO$ nanostructures for energy applications *J. Mater. Res.* **2019** 34, 3173-3185.

[27] Y. Li, X. Zhao, H. Liu, W. Li, X. Wang, Synthesis and Morphology Control of Nanoporous Cu_2O/Cu and Their Application as Electrode Materials for Capacitors *Nanomaterials (Basel)* **2019** 9.

[28] R. Guo, Y. Yu, Z. Xie, X. Liu, X. Zhou, Y. Gao, Z. Liu, F. Zhou, Y. Yang, Z. Zheng, Matrix-Assisted Catalytic Printing for the Fabrication of Multiscale, Flexible, Foldable, and Stretchable Metal Conductors *Adv. Mater.* **2013** 25, 3343-3350.

[29] P. Zhang, L. Li, D. Nordlund, H. Chen, L. Fan, B. Zhang, X. Sheng, Q. Daniel, L. Sun, Dendritic core-shell nickel-iron-copper metal/metal oxide electrode for efficient electrocatalytic water oxidation *Nat. Commun.* **2018** 9, 381.

[30] F. Urbain, P. Tang, N.M. Carretero, T. Andreu, J. Arbiol, J.R. Morante, Tailoring Copper Foam with Silver Dendrite Catalysts for Highly Selective Carbon Dioxide Conversion into Carbon Monoxide, *ACS Appl. Mater. Inter.* **2018** 10, 43650-43660.

[31] N. Torto, T. Ruzgas, L. Gorton, Electrochemical oxidation of mono- and disaccharides at fresh as well as oxidized copper electrodes in alkaline media *J. Electroanal. Chem.* **1999** 464, 252-258.

[32] H.Y.H. Chan, C.G. Takoudis, M.J. Weaver, Oxide Film Formation and Oxygen Adsorption on Copper in Aqueous Media As Probed by Surface-Enhanced Raman Spectroscopy *J. Phys. Chem. B* **1999** 103, 357-365.

[33] H.-H. Strehblow, V. Maurice, P. Marcus, Initial and later stages of anodic oxide formation on Cu, chemical aspects, structure and electronic properties *Electrochim. Acta* **2001** 46, 3755-3766.

[34] D. Yu, K. Goh, H. Wang, L. Wei, W. Jiang, Q. Zhang, L. Dai, Y. Chen, Scalable synthesis of hierarchically structured carbon nanotube–graphene fibres for capacitive energy storage *Nat. Nanotechnol.* **2014** 9, 555-562.

[35] Q. Liu, L. Zang, C. Yang, C. Wei, J. Qiu, C.-j. Liu, X.J.J.o.T.E.S. Xu, A Flexible and Knittable Fiber Supercapacitor for Wearable Energy Storage with High Energy Density and Mechanical Robustness *J. Electrochem. Soc.* **2018** 165.

[36] P. Wang, X. Du, X. Wang, K. Zhang, J. Sun, Z. Chen, Y. Xia, Integrated fiber electrodes based on marine polysaccharide for ultrahigh-energy-density flexible supercapacitors, *J. Power Sources* **2021** 506, 230130.